EAI Endorsed Transactions
on Scalable Information Systems
Research Article EAI.EU

Dynamic constitutive analysis of aluminum alloy materials commonly used in railway vehicles big data and its application in LS-DYNA

Juxing Liang[1,*], Jia Sun[1] and Wei Wei[2,*] and Rashid Ali Laghari[3]

[1]CRRC Nanjing Puzhen Co., Ltd. Nanjing 210000 China
[2]School of Mechatronics Engineering, Harbin Institute of Technology, Harbin 150001 China
[3]College of Mechanical and Electrical Engineering, Nanjing University of Aeronautics and Astronautics, Nanjing, 210016, China
Email:juxxi741@126.com; jiasun1985@163.com;tengtengout@qq.com;rashidali@nuaa.edu.cn
Corresponding author: Juxing Liang and Wei Wei (juxxi741@126.com;tengtengout@qq.com).

Abstract

The mechanical test for the three commonly used aluminum alloy materials (6005A-T6, 6008-T6 and 6082-T6) for rail vehicle big data are carried at different temperatures and different strain rates in this study. It can be seen that there are significant difference mechanical properties for these aluminum alloy. The main differences between them are the sensitivity of the strain rate and temperature. 6008-T6 and 6005A-T6 alloys have lower sensitivity to strain rate, while 6082-T6 alloy has higher sensitivity to strain rate and temperature. Based on the experimental data, the two commonly used dynamic material models of LS-DYNA, the Cowper-Symonds constitutive model and the Johnson-Cook constitutive model, are fitted. And then the two constitutive models are verified and compared by the dropping hammer impact test of the anti-climbing device. The results show that the Cowper-Symonds constitutive model has higher accuracy.

Keywords: big data, Dynamic constitutive model, Aluminum alloy for vehicle, Anti-climbing device dropping hammer impact test.

Received on 18 September 2021, accepted on 28 September 2021, published on 28 September 2021

Copyright © 2021 Juxing Liang *et al.*, licensed to EAI. This is an open access article distributed under the terms of the Creative Commons Attribution license, which permits unlimited use, distribution and reproduction in any medium so long as the original work is properly cited.

doi: 10.4108/eai.28-9-2021.171169

1. Introduction

With the rapid development of economy, people need higher requirements and expectations for efficient and high-quality life. Traffic travel is an important part of basic living needs, high speed, high stability and high safety have always been the main goals of improving traffic environment [1,2]. Nowadays, the process of urbanization is accelerated, and the connection between cities is increasingly close. The urban circle and economic belt have higher requirements for transportation. Rail transit is the most important way to realize the people movement and material transportation within and between cities. Its high efficiency and stable operation are the dependence of urban operation [3]. Because of the important role of rail vehicle, its safety has always been the main content of people's attention. Looking back at the development of rail transportation in recent years, numerous traffic accidents have also occurred, they even cause serious casualties and economic losses, and give

a bad impact on the society [4,5]. To improve the operation safety of rail vehicles is the top priority for its future technological improvement and industrial upgrading.

Vehicle body material selection and structure design are important factors affecting the safety. Crashworthiness assessment is usually carried out on the designed vehicle body to identify the safety degree of the designed vehicle model [6,7]. Vehicle crashworthiness refers to the ability to protect the safety of the vehicle body and its occupants in the event of a collision. In the crashing process, the material of the vehicle body is subjected to instantaneous crashing load and deforms greatly [8]. Since the end of last century, many scholars and designers have carried out a lot of researches on the crashworthiness of vehicles. At the same time, the International Railway Union standard system, the European Union standard system and the American standard system all have relevant provisions on the crashworthiness of vehicles [9,10]. Yu et al. [11] designed an anti-climbing and energy-absorbing device for rail vehicles and conducted a comprehensive evaluation of its crashworthiness. They used the method of combining simulation analysis with crash test, and then proved its excellent crashworthiness effect. Kumar et al. [12] studied the crashworthiness of a metal composite material widely used in vehicle body structure, and carried out an in-depth study and discussion on the deformation and crushing process of the sample. Paz et al. [13] studied the crashworthiness of the thin walled tubular parts used to enhance the protective effect in the case of vehicle collision, analyzed the collapse process under axial load by combining analytical formulas, numerical simulation and theoretical models, and quantified the crashworthiness from different sources. It can be seen that there are many methods for crashworthiness evaluation, many of them are based on the strength analysis of vehicle body materials.

For the analysis of dynamic mechanical properties of materials, researchers have done a lot of researches. Naik et al. [14] studied the mechanical properties of composites at high strain rates under tensile loading. They proposed an analytical formula to predict the tensile strength at medium and high strain rates, and the correctness of the formula was verified by comparing with the existing experimental data. Li et al. [15] developed an experimental device for DIC strain measurement based on high-speed and high thermal deformation, aiming at the problem of unclear calibration of strain and strain rate caused by temperature gradient in material tensile experiment. The parameter identification of constitutive model under the condition of internal hot stamping could provide more accurate basis. Tano et al. [16] established a numerical model to analyze the interfacial strain state in view of the tensile properties of composite materials for construction engineering. At present, the numerical simulation method has become an important technical means to study the crashness of railway vehicles. However, since the influence of material constitutive model expression on the simulation results is far greater than the influence of computer program algorithm error, the research on material dynamic constitutive model becomes extremely critical.

The constitutive model of materials is an important way to characterize the dynamic mechanical properties of materials, which is of great significance to the study of deformation, fracture and cutting characteristics of materials. Zhu et al. [17] studied the mechanical properties of 42CrMo steel commonly used for high-speed train axles and analyzed its quasi-static compression behavior under three different strain rates. Based on the Zerilli-Armstrong constitutive model and the quasi-static, dynamic compression experiments, a new constitutive model considering the thermal softening effect is proposed. Xue et al. [18] established a strengthened constitutive model to describe the hysteretic characteristics and variable stiffness behavior of elastic porous metal rubber materials. Then he analyzed and discussed its anisotropy and dynamic characteristics related to stiffness and energy dissipation. Shokrieh et al. [19] established a dynamic constitutive mesomechanical model to predict the strain rate related mechanical behavior of laminated glass/epoxy composites, and obtained a good agreement with the experimental results. The constitutive model with high fitting degree is very important to fully understand the material and analyze its mechanical properties. This paper is organized as follows. In section 2, we introduce the common variable rate tensile test. Section 3 and section 4 display the constitutive equation fitting and dropping hammer impact test and results of anti-creeper. Section 5 fives the finite element analysis and constitutive equation verification. There is a conclusion in section 6.

2. Common variable rate tensile test

2.1. Test method and instrument

In order to obtain the constitutive equation of aluminum alloy for rail vehicle, it is necessary to collect its stress-strain characteristic curve to obtain effective data [20-24]. At present, constant strain rate tensile test is usually used to collect mechanical properties data of materials. In this paper, the tensile test is divided into two parts including the quasi-static tensile test and dynamic tensile test. Digital Imaging Correlation (DIC) is used to record the whole test process.

2.2. Quasi-static tensile test

The quasi-static tensile test is carried out according to GB/T 228.1-2010 standard. The strain rate is fixed at 0.001/s during stretching process. Each specimen is stretched at 25℃, 50℃ and 100℃ respectively, and the tensile effects

under different temperature conditions are compared to explore the influence of temperature factors on the material constitutive model [25]. Three tensile tests are carried out under each test condition, and the results are averaged to eliminate the occasional experimental errors. The size diagram of the specimen used in the quasi-static tensile experiment is shown in Figure 1(a). The overall length of the specimen is 200mm, the width is 35mm, and the thickness varies according to different materials.

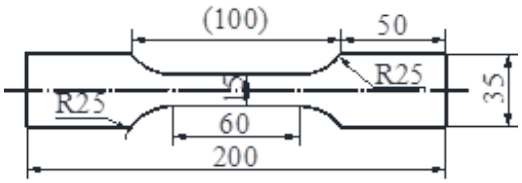

(a)Quasi-static tensile test specimen

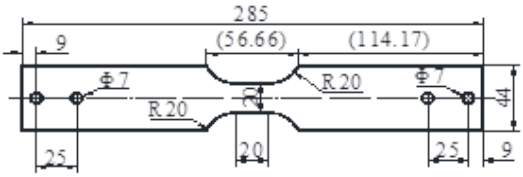

(b)Dynamic tensile test specimen

Figure 1. Size of specimens used in tensile tests.

1) Dynamic tensile test

The dynamic tensile test in this study is conducted according to the GBT 30069.2-2016 standard. The test process is conducted on ZwickRoell HTM 16020 high speed electro-hydraulic servo test machine. For different material samples, the tensile test is completed at eight strain rate levels, namely 0.001/s, 0.1/s, 1/s, 10/s, 100/s, 200/s and 400/s. Five tests are carried out under each strain rate condition, and the experimental data are averaged to study the effect of strain rate on the constitutive model of the material. The sample size diagram for dynamic tensile test is shown in Figure 1(b). The length of the sample is 285mm and the width is 44mm. The thickness of the sample varies according to different materials.

2) DIC measuring equipment

Since the collected stress and strain data are to be used in the fitting of the material constitutive equation, it is necessary to record the whole process of stress and strain changes in the quasi-static and dynamic tensile tests. DIC technology is used to record the emergency situation. Before the test, high speed camera, high speed light source and shade plate are installed, and the specimen is fixed on the clamp head of the testing machine. An Photron SA-Z high-speed camera is used to collect the full-field deformation information of the specimen, and DIC method is used to obtain the stress-strain curve of the material, as shown in Figure 2.

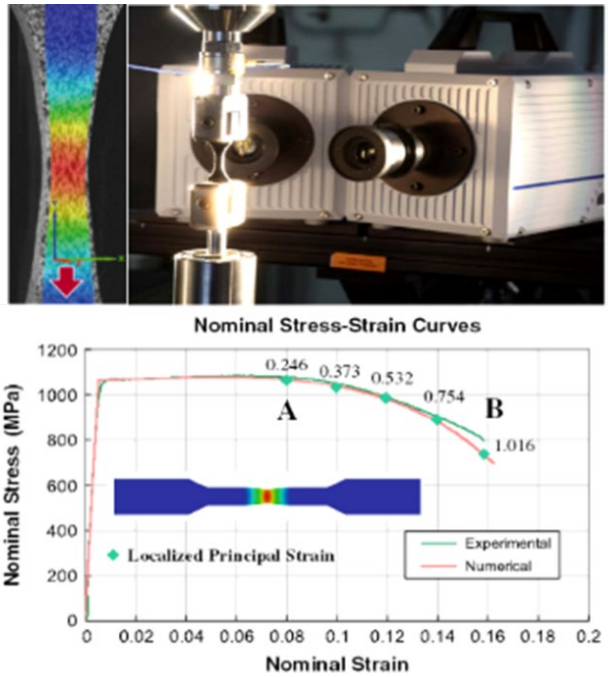

Figure 2. Digital image correlation test system.

2.3. Test material

In this paper, three kinds of aluminum alloy materials commonly used in rail vehicle body are used for experimental research, they are 6005A-T6, 6008-T6 and 6082-T6 respectively. The composition of these materials is shown in Table 1. Next, the tensile test and constitutive model will be constructed. Thickness of different types of aluminum alloy samples is different, 6005A-T6 thickness is 4mm, 6008-T6 and 6082-T6 thickness are 5mm.

Table 1. Three material compositions.

Composition	Si	Fe	Cu	Mn	Mg	Cr	Zn	Ti	Al
6005A-T6	0.7	0.35	0.25	0.5	0.6	0.3	0.2	0.1	margin
6008-T6	7	0.35	0.3	0.3	0.6	0.3	0.2	0.1	margin
6082-T6	1.0	0.5	0.1	0.7	0.9	0.25	0.2	0.1	margin

2.4. Experimental results and discussion

The engineering stress-strain relationships of four kinds of metals are obtained through the quasi-static and dynamic tensile tests with several groups of samples under different parameters. The real stress-strain relationship of the test needs to be calculated from the engineering stress-strain formula, which is as follows:

$$\sigma_T = (1 + \varepsilon_E)\sigma_E \quad (1)$$

$$\varepsilon_T = \ln(1 + \varepsilon_E) \quad (2)$$

Where σ_T , σ_E , ε_T and ε_E are the true stress, engineering stress, true strain and engineering strain respectively.

The real stress-strain curves of 6005A-16 at different strain rates and temperature parameters are shown in Figure 3. The yield strength of 6005A-16 is higher than that of 5083-H11 aluminum alloy. With the increase of strain rate, the yield strength of 6005A-T6 material increases continuously. When the strain rate is 0.001/s, the yield strength is 220MPa. When the strain rate increases to 400/s, the yield strength increases to 275MPa. The strain rate has little effect on the fracture strength of aluminum alloy 6005A-T6, which varies from 295 MPa to 330MPa. The failure strain also varies with the strain rate, rising from 0.105 at 0.001/s to 0.15 at 400/s. Temperature has little effect on the yield strength of this material. When the temperature is 25℃ and 50℃, the real stress-strain curves are basically similar before reaching the failure strain. However, when the temperature reaches 100℃, the fracture strength of the material decreases and the failure strain increases.

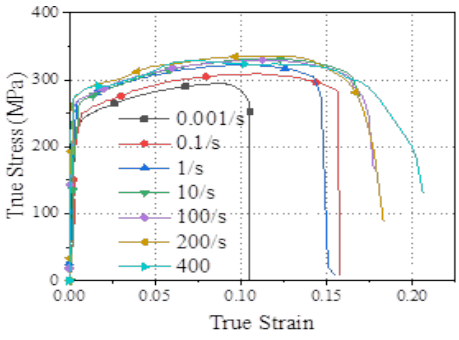

(a)Different strain rates at 25℃

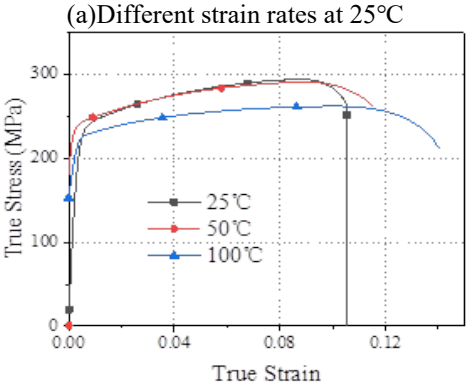

(b) Different temperature at 0.001/s

Figure 3. True stress-strain curve for 6005A-T6.

The real stress-strain curves of 6008-T6 at different strain rates and temperature parameters are shown in Figure 4. With the increase of strain rate, the yield strength of 6008-T6 material increases first and then decreases. When the strain rate is 0.001/s, the yield strength is 145MPa. When the strain rate is increased to 200/s, the yield strength reaches the maximum value with 200MPa. When the strain rate reaches to 400/s, the yield strength decreases to 155MPa. The strain rate has a certain effect on the fracture strength of aluminum alloy 6008-T6. With the increase of strain rate, the fracture strength increases from 270 to 315MPa. The failure strain also increases first and then decreases, rising from 0.19 at 0.001/s to 0.24 at 200/s, and then dropping to 0.22 at 200/s. Temperature has little effect on the yield strength of the material, but has some effect on the fracture strength. The fracture strength is 280MPa at the temperature of 25℃ and 50℃. However, when the temperature reaches 100℃, the fracture strength of the material decreases to 248MPa and the failure strain increases.

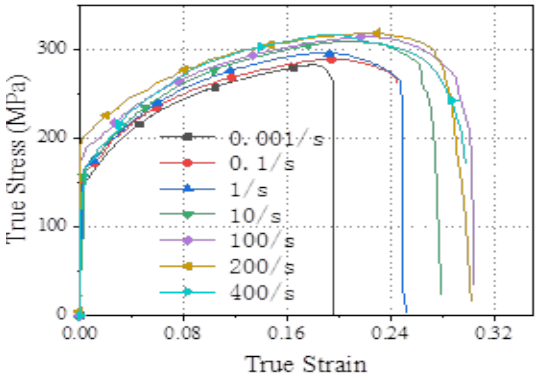

(a)Different strain rates at 25℃

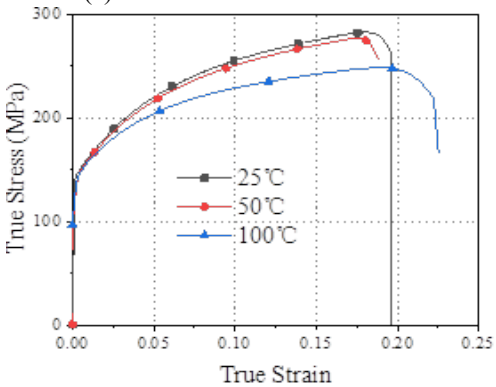

(b) Different temperature at 0.001/s

Figure 4. True stress-strain curve for 6008-T6.

The real stress-strain curves of 6082-T6 at different strain rates and temperature parameters are shown in Figure 5.

With the increase of strain rate, the yield strength of 6082-T6 material increases gradually. When the strain rate is 0.001/s, the yield strength is 300MPa. When the strain rate is increased to 400/s, the yield strength reaches the maximum value with 355MPa. The strain rate has a certain effect on the fracture strength of aluminum alloy 6082-T6. With the increase of strain rate, the fracture strength increases from 340MPa to 400MPa and then decreases to 375MPa. The failure strain is first increased and then decreased. Temperature has a great influence on the yield strength and the fracture strength of the material. When the temperature is 25℃ and 50℃, the fracture strength of the material is 340MPa, while when the temperature reaches to 100℃, the fracture strength of the material is reduced to 300MPa, and the failure strain increases.

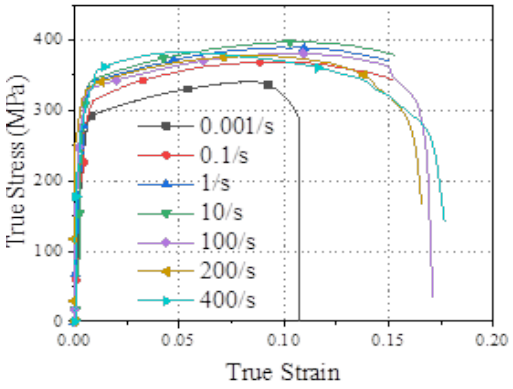

(a)Different strain rates at 25℃

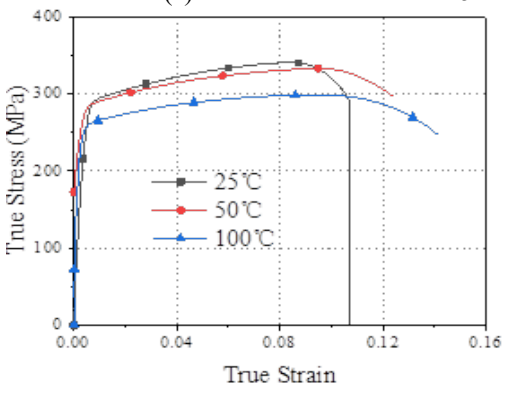

(b) Different temperature at 0.001/s

Figure 5. True stress-strain curve for 6082-T6

Based on the above experimental results, it is found that different types of aluminum alloy materials have great differences in mechanical properties, and their sensitivity to strain rate and temperature are also different. The sensitivity of 6008-T6 and 6005A-T6 to strain rate is low, while the sensitivity of 6082-T6 to strain rate and temperature is high. For different types of aluminum alloy materials, the constitutive equations also have great differences.

3. Constitutive equation fitting

The real stress-strain curves are used to fit the constitutive equations of three aluminum alloy materials. In this study, Johnson-Cook constitutive model and Cowper-Symonds constitutive model, which are commonly used in metal impact research, are selected. The two constitutive models are often used in simulation.

The Cowper-Symonds constitutive equation can be expressed as:

$$\dot{\varepsilon} = D(\frac{\sigma_0^d - 1}{\sigma_0})^q \tag{3}$$

Wherein, σ_0 is the static flow stress. σ_0^d is the static flow stress corresponding to $\dot{\varepsilon}$. D and q are the material parameters, which can be obtained by fitting.

The Johnson-Cook constitutive equation can be expressed as:

$$\sigma = (\sigma_0 + B\varepsilon^n)(1 + C\ln\frac{\dot{\varepsilon}}{\dot{\varepsilon}_0})(1 - T^{*m}) \tag{4}$$

Where T^* is the dimensionless temperature coefficient, $T^* = \frac{T - T_r}{T_m - T_r}$. T_r is the reference temperature. σ_0 is the stress measured at this temperature. $\dot{\varepsilon}_0$ is the reference strain rate, $\dot{\varepsilon}_0$=1/s. The five parameters in this constitutive σ_0, B, C, n, mcan be obtained by fitting.

Johnson-Cook constitutive equation is widely used in the study of dynamic constitutive relations of materials. Compared with the Cowper-Symonds constitutive, the Johnson-Cook constitutive equation takes into account the influence of temperature on the material. Origin software is used to fit the measured real stress-strain curves and synthesizing the above two constitutive models. The relevant parameters under the two constitutive models are shown in Table 2.

Table 2. Three material constitutions

	C-S constitution parameter		J-C constitution parameter					
	D	q	σ_0	B	n	C	m(50 ℃)	m(100℃)
6005A-T6	5.47104	7.7	242	216.667	0.5187	0.00261	1.1352	1.084
6008-T6	5.8182	5.373	150.0	348.6	0.532	0.012	1.2744	1.15296

	8			9		37	
6082-T6	9.50518	6.3776	302	165.857	0.51006	0.00491	0.71979	0.82278

4. Dropping hammer impact test and results of anti-creeper

The test is completed on a dropping hammer tester built by Harbin Institute of Technology. Dropping hammer test specimens are shown in Figure 6. The side of the anti-climbing board is in the shape of "mountain", and the material is 6005A-T6. There are six energy absorption tubes, the material is 6008-T4. The mounting plate is a rectangular plate, and the material is 6082-T6. The peak impact force and holding time are recorded, the amount of deformation is measured and the average buffer force is recorded.

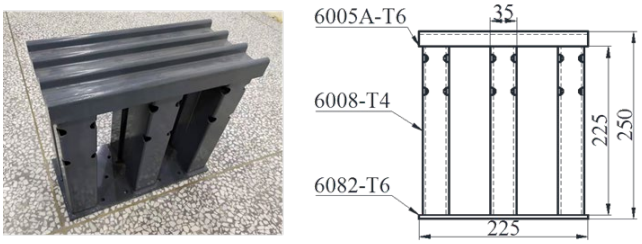

Figure 6. Dropping hammer test specimen size and material

Dropping hammer impact test system mainly includes falling hammer (counterweight), guide rail, release mechanism, high-speed photography, force sensor, test bench, specimen tools and so on. The installation of the specimen is shown in Figure 7. The anti-climbing device is installed on the test bench, located directly below the dropping hammer, and placed in the center.

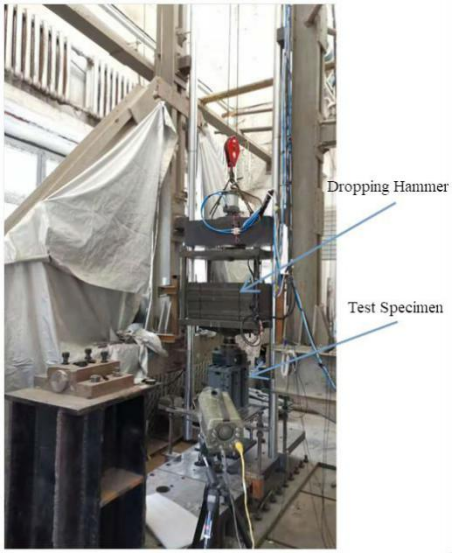

Figure 7. Site installation drawing of the specimen

The dropping hammer is lifted at different heights to obtain different impact velocity and impact energy. In this dropping hammer test, a total of 3 impacts are carried out on a test piece. The parameters and results of each impact test are shown in table 3. The obtained test curve is shown in figure 8.

Table 3. Statistical analysis of test results.

No.	Lifting height/m	Velocity(km/h)	H1/mm	H2/mm	ΔH/mm	Average buffering power/kN	Peakbuffering power/kN
1-1	2.46	25	400	372	28	--	--
1-2	2.46	25	372	349	23	647	917
1-3	3.5	30	349	303	46	626	880
1-4	5.1	36	303	240	63	624	943

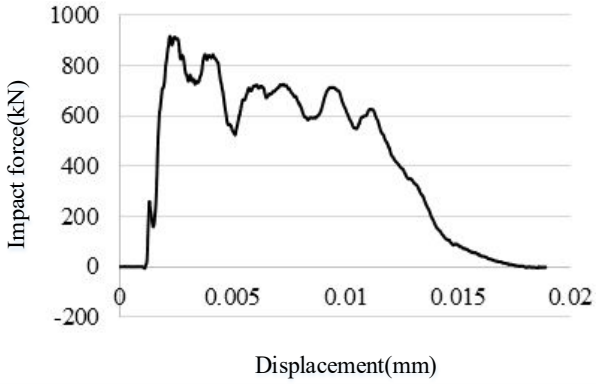

(a)The second impact force - time history curve.

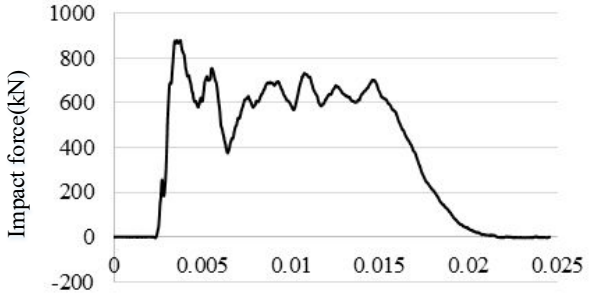

(b)The third impact force - time history curve.

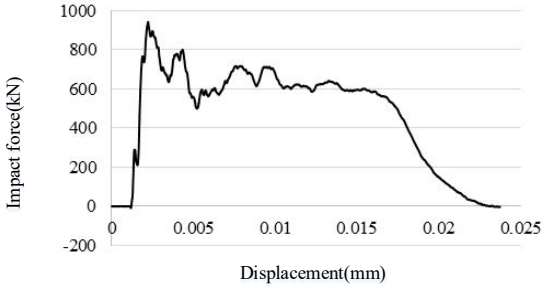

(c) The fourth impact force - time history curve.

Figure 8. Impact force - time history curve of anti-creep

After four impacts, the deformation morphology of the specimen is shown in figure 9. It can be seen that the deformation amount of each energy absorption tube is relatively consistent after deformation. It is shown that the impact force can be uniformly transferred to each energy absorption tube in the impact test process, and there is no bias load phenomenon in the impact process.

(a)Before test

(b) after test

Figure 9. Comparison before and after the anti-climbing device test

5. Finite element analysis and constitutive equation verification

In order to verify the applicability of the two constitutive models, a dropping hammer test is carried out on the anti-climbing absorber for high-speed train constructed of the four aluminum alloy materials. The obtained constitutive equation is applied to LS-DYNA finite element simulation. By comparing force-displacement and force-time curves, the applicability of the fitted constitutive in the process of vehicle material deformation is verified.

LS-DYNA is used to simulate the dropping hammer test. The simulation is divided into two groups. In the first group, all aluminum alloys are subjected to the 98* MAT_SIMPLIFIED_JOHNSON_COOK constitutive, which ignores the influence of temperature on the constitutive model of Johnson-Cook, and thus it is more consistent with the dropping hammer impact test. In the second group, the 24*MAT_PIECEWISE_LINEAR_PLASTICITY material with Cowper-Symonds constitutive model is used for all the aluminum alloys, and the material parameters are all the same as the constitutive obtained from the previous fitting. Other boundary conditions in the two groups of simulations are the same. In the simulation, 20*MAT_RIGID material is used for the dropping hammer. The energy-absorbing pipe fittings are modeled by 4-node quadrilateral shell elements.

The upper-lower plates and the dropping hammer are modeled by 8-node hexahedral mesh, and the mesh size is unified to 5mm. Displacement constraints in x, y, and z directions and rotation constraints around x, y, and z axes are applied below the model. It uses the #4 hourglass control method on the whole structure to reduce the hourglass energy in the calculation. *CONTACT_AUTOMATIC_SINGLE SURFACE is used for the contact mode in LS-DYNA. This method can automatically search the contact element, and at the same time, the thickness of shell element is taken into account in the contact calculation. We set THKCHK to 1 in the *CONTROL_CONTACT keyword, that is, the variation of shell element thickness is taken into account in the calculation. Sensors are added to the model to record the force between the dropping hammer and the anti-climb board. The whole process of impact from dropping hammer to spring is simulated, and the impact force-time curve is recorded in the simulation.

A. J-C constitutive simulation results and analysis

Figure 10 shows the simulation results based on the J-C constitutive. It can be seen that although the simulated results have some errors in capturing the shape of the deformed energy absorption tube, on the whole, the deformation reflected by the simulation is mainly concentrated on the energy absorption tube, while neither the anti-climbing plate nor the mounting plate has significant deformation, which is consistent with the observed results in the experiment. It is worth noting that, based on the simulation of J-C constitutive, the deformation of the energy absorption tube is mainly concentrated in the upper position where it contacts with the anti-climbing plate, while there is no deformation at the position where it is connected with the mounting plate. The simulation results of the corresponding impact-time history curve are compared with the test results, as shown in Figure 11.

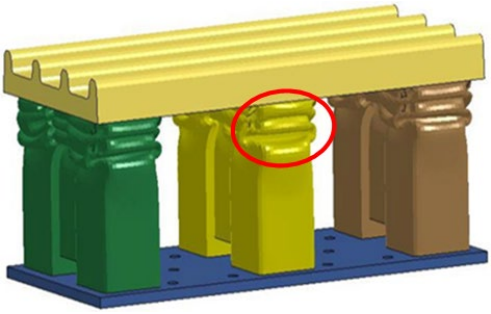

Figure 10. Anti-creep deformation process

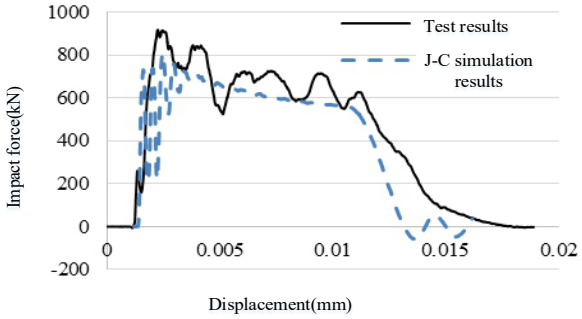

(a)The second test impact force - time history curve comparison

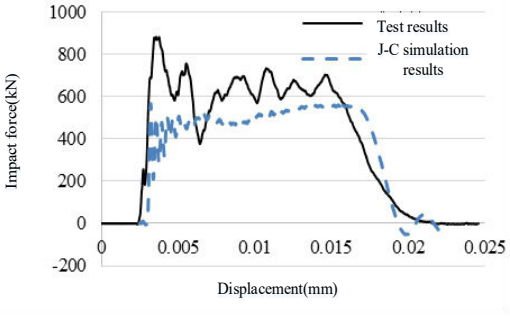

(b)The third test impact force - time history curve comparison

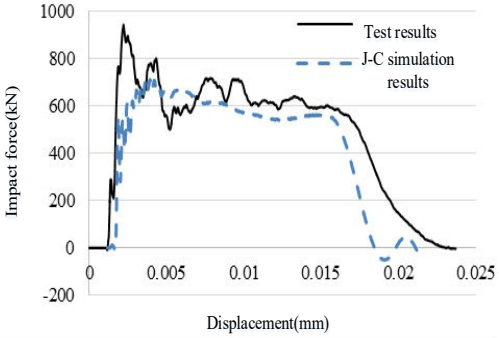

(c)The third test impact force - time history curve comparison

Figure 11. Impact-time history curve of J-C constitutive model

According to Table 4, the error between the simulation results of the third, fourth impact peak force and the test value is greater than 35%. The error between the simulation results of the second peak impact force and the test value is less than 20%. The error between the simulation results of the second, fourth impact average buffering force and the test value is less than 5%. However, the error between the simulation result of the third impact average buffering force and the test value is large, reaching about 20%. The time holding error is more than 10% in three impact simulations. The error between the simulation results of the second, third

impact deformation and the test value is more than 20%, and the error of the fourth impact is less than 5%.

Table 4. J-C simulation and test comparison.

Test number		Test result	Simulation result	Error/%
1-2	Peak force/kN	917	756	17.56
	Average buffering force /kN	647	610	5.72
	Holding time/ms	17.1	12.6	26.32
	Deformation/mm	23	31	-34.78
1-3	Peak force/kN	880	564	35.91
	Average buffering force /kN	626	502	19.81
	Holding time/ms	19.7	17.7	10.15
	Deformation/mm	46	57	-23.91
1-4	Peak force/kN	943	592	37.22
	Average buffering force /kN	624	594	4.81
	Holding time/ms	22.4	18.1	19.2
	Deformation/mm	63	65	-3.17

B. C-S constitutive simulation results and analysis

Figure 12 shows the simulation results based on the C-S constitutive. Similar to the results of J-C constitutive simulation, there is also a certain error in capturing the shape of the energy absorption tube after deformation. It is worth noting that, compared with the simulation results of J-C constitutive, it can be found that C-S constitutive can not only capture the deformation of the upper position in contact with the anti-climbing plate, but also better capture the deformation of the position connected with the mounting plate. This indicates that the C-S constitutive model has higher accuracy in the case of dropping hammer impact deformation of anti-climber. The simulation results of the corresponding impact-time history curve are compared with the test results, as shown in Figure 13.

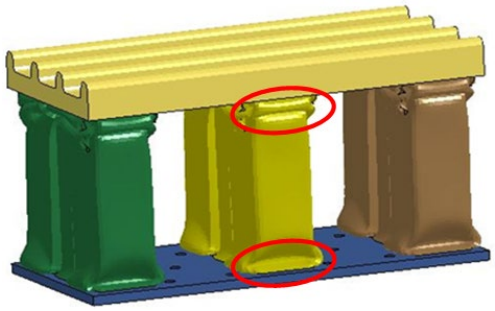

Figure 12. Anti-climber deformation result.

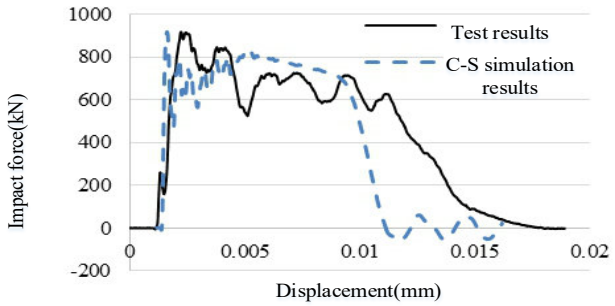

(a)The second test impact force - time history curve comparison

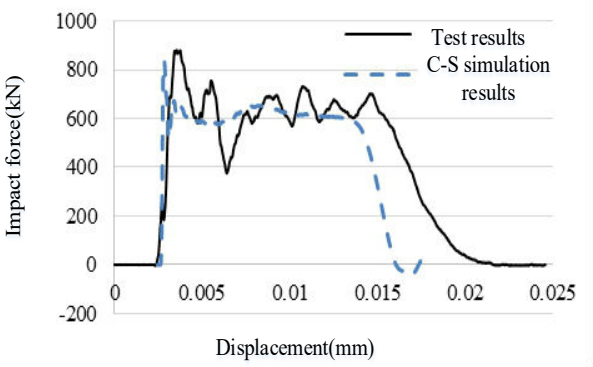

(b)The third test impact force - time history curve comparison

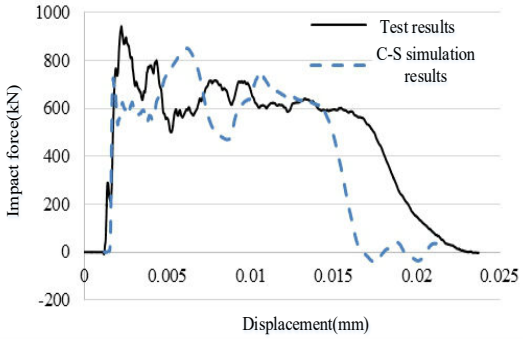

(c)The third test impact force - time history curve comparison

Figure 13. Impact-time history curve of C-S constitutive model

It can be seen from Table 5 that the error between the simulation results of the second, third impact peak force and the test value is small, which is less than 10%. However, the error between the simulation results of the fourth impact peak force and the experimental value is large, reaching about 25%. The error between the simulation results of the third, fourth shocks and the experimental values is less than 5%. However, the error between the simulation result and the test value of the second impact average buffering force is larger, reaching about 14%. The time holding error is more than 25% in three impact simulations. The error trend of the deformation is similar to that of the average buffering force. The error between the simulation results of the third, fourth impact deformation and the experimental values is less than 5%. The second impact error reaches about 13%. Compared with J-C constitutive simulation results, C-S constitutive simulation results have higher accuracy.

Table 5. C-S simulation and test comparison.

Test number		Test result	Simulation result	Error/%
1-2	Peak force/kN	917	897	2.18
	Average buffering force /kN	647	737	-13.91
	Holding time/ms	17.1	10.8	36.84
	Deformation/mm	23	26	-13.04
1-3	Peak force/kN	880	834	5.23
	Average buffering force /kN	626	613	2.08
	Holding time/ms	19.7	14.3	27.41
	Deformation/mm	46	44	4.35
1-4	Peak force/kN	943	705	25.24

Average buffering force /kN	624	643	-3.04
Holding time/ms	22.4	16.1	28.13
Deformation/mm	63	60	4.76

6. Conclusions

Through the above analysis, we can draw the following conclusions:

- Through the analysis of the experimental results, it is found that the mechanical properties of different types of aluminum alloy materials are greatly different, and the sensitivity to strain rate and temperature are also different. The sensitivity of 6008-T6 and 6005A-T6 to strain rate is low, while the sensitivity of 6082-T6 to strain rate and temperature is high.
- The Cowper-Symonds constitutive model and Johnson-Cook constitutive model, two material models commonly used in finite element software LS-DYNA, are fitted to obtain the constitutive equation parameters.
- The two constitutive models are verified and analyzed through the anti-creep drop impact test, and it is found that although the Cowper-Symonds constitutive model and the Johnson-Cook constitutive model both have certain errors in capturing the deformation of the energy absorption tube, the C-S model has better performance in capturing the overall deformation of the energy absorption tube. Compared with the Johnson-Cook constitutive model, the Cowper-Symonds constitutive model also has higher accuracy in capturing the key parameters of impact experiments. In the future, we will research the more advanced aluminum alloy materials commonly in railway vehicles big data and its application in LS-DYNA.

References

[1] Landry S, Jeon M, Lautala P, et al. Design and assessment of in-vehicle auditory alerts for highway-rail grade crossings. Transportation research, 2019, 62F, pp. 228-245.

[2] Ning B, Xun J, Gao S, et al. An Integrated Control Model for Headway Regulation and Energy Saving in Urban Rail Transit. IEEE Transactions on Intelligent Transportation Systems, 2015, 16(3), pp. 1469-1478.

[3] Bhardawaj S, Sharma R C, Sharma S K. Development in the modeling of rail vehicle system for the analysis of lateral stability. Materials today: proceedings, 2019, 25. pp. 610-619.

[4] Hadj-Mabrouk H. Application of case-based reasoning to the safety assessment of critical software used in rail transport. Safety Science, 2020, 131, pp. 104928.

[5] SUN Qian, WEN Yongpeng, JI Zhonghui, ZOU Yu. Modeling and simulation of composite vibration absorber for urban rail vehicle body. JOURNAL OF VIBRATION AND SHOCK, 2020, 39(21): 203-210.

[6] Olmos J, Astiz M. Non-linear vehicle-bridge-wind interaction model for running safety assessment of high-speed trains over a high-pier viaduct. Journal of Sound and Vibration. 2018, 419: 63-89.

[7] Isaac C. Crashworthiness performance of green composite energy absorbing structure with embedded sensing device providing cleaner environment for sustainable maintenance. Sustainable Materials and Technologies, 2020, 25: e00196.

[8] Abdullah N, Sani M, Salwani M, et al. A review on crashworthiness studies of crash box structure[J]. Thin-Walled Structures, 2020, 153: 106795.

[9] YUAN Wen-jing, CHENG Jian-feng, WANG Qian-xuan, ZHOU Wei. Research on and Application of an Independent Safety Assessment Evaluation Method for Rail Transit Vehicles. Journal of Wuyi University (Natural Science Edition), 2020, 34(4), pp. 29-35. (in Chinese)

[10] LIU Zhengdong, YANG Jin, WANG Chengguo, YU Zengming. Based on Whole Lifecycle and Risk-oriented Method of ISA of Railway Signal System[J]. Railway Computer Application, 2016, 25(10): 16-20.

[11] Yu Qingsong , Xue Jinbo, Liu Yanwen. Research on Crashworthiness of New Large Capacity Anti-climbing Energy Absorber for Railway Vehicles. Industrial Technology Innovation, 2019, 6(2), pp. 101-105. (in Chinese)

[12] Kumar A, Shunmugasundaram M, Sivasankar S, et al. Evaluation of axial crashworthiness performance of composite wrapped metallic circular tubular structures[J]. Materials Today-Proceedings, 2020, 27:1268-1272.

[13] Paz J, Díaz J, Romera L. Analytical and numerical crashworthiness uncertainty quantification of metallic thin-walled energy absorbers [J]. Thin-Walled Structures, 2020, 157: 107022.

[14] Kumar M, Naik N. Prediction of mechanical behavior of composites under high strain rate tensile loading[J]. Mechanics Research Communications, 2018, 90: 1-7.

[15] Li Y, Li H, Chen Y, et al. Constitutive parameters identification based on DIC assisted thermo-mechanical tensile test for hot stamping of boron steel[J]. Journal of Materials Processing Technology, 2019, 271: 429-443.

[16] Tano B, Dias D, Fowmes G, et al. Numerical modeling of the nonlinear mechanical behavior of multilayer geosynthetic system for piggyback landfill expansions[J]. Geotextiles & Geomembranes, 2016, 44: 782-798.

[17] Zhu Z, Lu Y, Xie Q, et al. Mechanical properties and dynamic constitutive model of 42CrMo steel[J]. Materials & Design, 2017, 119: 171-179.

[18] Xue X, Ruan S, Bai H, et al. An enhanced constitutive model for the nonlinear mechanical behavior of the elastic-porous metal rubber[J]. Mechanics of Materials, 2020, 148: 103447.

[19] Shamaei A, Shokrieh M, Seyedalikhani. A novel dynamic constitutive micromechanical model to predict the strain rate dependent mechanical behavior of glass/epoxy laminated composites[J]. Polymer Testing, 2020, 82: 106292.

[20] Laghari RA, Li J, Laghari AA, Wang S (2020) A Review on Application of Soft Computing Techniques in Machining of Particle Reinforcement Metal Matrix Composites. Arch Comput Methods Eng 27:1363–1377.

[21] Li J, Laghari RA (2019) A review on machining and optimization of particle-reinforced metal matrix composites. Int J Adv Manuf Technol 100:2929–2943.

[22] Laghari RA, Li J, Wu Y (2020) Study of Machining Process of SiCp/Al Particle Reinforced Metal Matrix Composite Using Finite Element Analysis and Experimental Verification. Materials (Basel) 13:5524

[23] Laghari RA, Li J, Mia M (2020) Effects of Turning Parameters and Parametric Optimization of the Cutting Forces in Machining SiCp/Al 45 wt% Composite. Metals (Basel) 10:840

[24] Laghari RA, Li J (2021) Modeling and optimization of cutting forces and effect of turning parameters on SiCp/Al 45% vs SiCp/Al 50% metal matrix composites: a comparative study. SN Appl Sci 3:706

[25] Shoulin Yin, Hang Li. Time-domain integration method of moments used for ultra wideband response of monopole antenna[C]// Progress in Electromagnetic Research Symposium. IEEE, 2016:1177-1180.